Electronic and thermoelectric transport in semiconductor and metallic superlattices

Daryoosh Vashaee and Ali Shakouri[a)]
Jack Baskin School of Engineering, University of California, Santa Cruz, California 95064

(Received 14 July 2003; accepted 29 October 2003)

A detailed theory of nonisothermal electron transport perpendicular to multilayer superlattice structures is presented. The current–voltage ($I-V$) characteristics and the cooling power density are calculated using Fermi–Dirac statistics, density-of-states for a finite quantum well and the quantum mechanical reflection coefficient. The resulting equations are valid in a wide range of temperatures and electric fields. It is shown that conservation of lateral momentum plays an important role in the device characteristics. If the lateral momentum of the hot electrons is conserved in the thermionic emission process, only carriers with sufficiently large kinetic energy *perpendicular* to the barrier can pass over it and cool the emitter junction. However, if there is no conservation of lateral momentum, the number of electrons participating in a thermionic emission will increase. This has a significant effect on the $I-V$ measurements as well as the cooling characteristics. Theoretical calculations are compared with the experimental dark current characteristics of quantum well infrared photodetectors and good agreement over a wide temperature range for a variety of superlattice structures is obtained. In contrast with earlier studies, it is shown that lateral momentum is conserved for the case of electron transport in planar semiconductor barriers. [DOI: 10.1063/1.1635992]

I. INTRODUCTION

Heterostructure integrated thermionic (HIT) coolers have been made and characterized for applications in both integrated cooling of optoelectronics and electronic devices (see Fig. 1).[1–9] In these structures, a potential barrier is used for the selective emission of hot electrons and the evaporative cooling of the electron gas. The HIT cooler is based on either a single barrier or a multi barrier structure. In a single barrier structure within a strong nonlinear transport regime, electron transport is dominated by the supply of electrons in the cathode layer.[1] Since only hot electrons (with energies larger than the Fermi energy, E_f) are emitted above the barrier, electron–electron and electron–phonon interactions try to restore the quasi Fermi distributions in the cathode layer by absorbing heat from the lattice, thus cooling the emitter. This heat is deposited on the anode side. Theoretical estimates[1,2,10] show that there is an optimal barrier width on the order of a few electron energy relaxation lengths and an optimum barrier height on the order of k_BT; such heterostructure coolers can provide between 20 and 30 °C cooling with kW/cm^2 cooling density. Since the operating currents for the device are very high (10^5 A/cm^2), nonideal effects such as Joule heating at the metal–semiconductor contact resistance, as well as heat sink with finite thermal resistance at the anode have limited the experimental cooling results to <4 °C.[3,11] For the case of multi barrier (superlattice) structures, significant cooling can be achieved at small biases in the linear transport regime.[12–14] A superlattice is chosen so that hot electrons move easily in the materials, and the movement of cold electrons is restricted. Thus there will be net cooling in the cathode layer and heating in the anode layer. Estimates show that a small barrier height on the order of k_BT does not give much improvement over bulk thermoelectric materials,[15–17] and it was suggested to use tall barriers and high doping densities to achieve a large number of electrons moving in the material.[4,18] In this article the latter regime of transport is investigated in detail and we show how conserving an electron's lateral momentum in thermionic emission plays an important role in device performance. There have been several recent theoretical studies of electron transport in single barrier and superlattice structures where thermionic emission and conventional thermoelectric cooling are compared.[15–17] These studies mainly focus on ballistic transport in thin barriers and do not consider the effect of lateral momentum conservation.

Figure 1 shows the energy diagram of a typical superlattice microcooler. Cooling power is proportional to the number of electrons involved in a thermionic emission. Only electrons with a kinetic energy in the z direction that is higher than the barrier height can pass over the barrier and participate in thermionic cooling. Assuming that the quantized energy levels in the quantum well are given by E_i, the number of electrons participating in transport perpendicular to barriers can be calculated according to

$$n_e(V)=\sum_{E_i}\int_{E_i}^{\infty}D(E)[f(E,E_f)-f(E,E_f-qV)]T(E)dE, \tag{1}$$

where $D(E)$ is the electron density of states, f is the Fermi–Dirac distribution, and $T(E)$ is the transmission probability for the electrons to pass the barrier. E_i is the quantized en-

a)Author to whom correspondence should be addressed; electronic mail: ali@soe.ucsc.edu

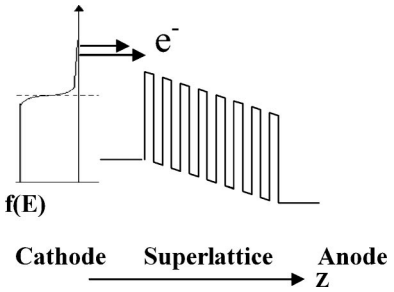

FIG. 1. Schematic energy diagram of a heterostructure integrated thermionic (HIT) microcooler along with electron energy distribution and the Fermi level.

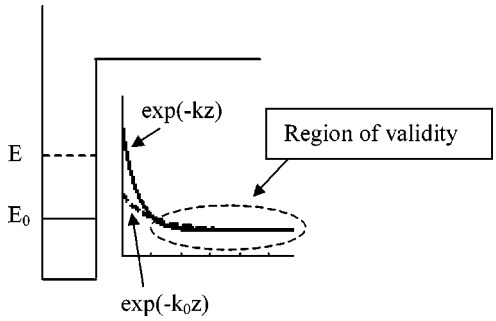

FIG. 2. Penetration of a quantum-well wave function into the confining barrier. In the absence of scattering, all the states belonging to the same subband E_0 decay asymptotically as proportional to $\exp(-k_0 z)$. In the presence of scattering, however weak, the asymptotic decay is proportional to $\exp(-kz)$ and depends on the in-plane kinetic energy. That is valid at a large distance from the well.

ergy level in the well. A similar expression is often used for the calculation of dark currents in quantum well infrared photodetectors (QWIPs);[19–25] however,[19] the term $(-f(E,E_f-qV))$ is ignored, because it is negligible when the Fermi level is deep in the well. In the case of HIT coolers, the Fermi level should be close to the barrier height in order to achieve large cooling powers. In the latter case, one should check for the availability of empty states at the neighboring well and the $(-f(E,E_f-qV))$ term should be included. While Eq. (1) accurately predicts the dark current in quantum well photodetectors (see Appendix and Ref. 19), one should consider several other important factors when calculating thermionic current and cooling power density for HIT coolers. Sections II and III describe various modifications to these calculations when the conservation of lateral momentum is considered.

II. ROLE OF LATERAL MOMENTUM

Since the transmission probability in Eq. (1), $T(E)$, depends on the total energy of the electron, it implies that equal energy states with a different k_z have the same contribution to the thermionic current. This is valid only when there is scattering. Without any scattering, electron motion in the z direction and in the x-y plane is decoupled. To account for the decoupling $T(E)$ should be replaced by $T(E_i)$ in Eq. (1), which means that the transmission probability depends on the quantized energy levels inside the well. This will significantly decrease the number of electrons passing the barrier. Meshkov[26] has studied the role of scattering in detail for the case of carrier tunneling in a barrier. In the absence of electron-electron interaction and inhomogeneities, the motion in the xy plane is completely separable from the quantized longitudinal motion, and electron wave function decays in the barrier with the characteristic exponential

$$\psi\alpha \exp\left(-\int dz\{2m[V(z)-E_i]\}^{1/2}/\hbar\right), \tag{2}$$

where $V(z)$ is the potential in the barrier, and E_i is the quantized electron energy in the well. This means that the kinetic energy $K=p^2/2m$ of the electron motion in the xy plane does not affect the tunneling exponent.

The situation will be different in the presence of scattering, which mixes different degrees of freedom. It has been shown by Meshkov[26] that however weak the scattering processes, the asymptotic decay law for the electron density is described by a wave function that results if the carriers tunnel in a one-dimensional potential $V(z)$ and have total energy $E=E_0+K$ in the exponent[21]

$$\psi\alpha \exp\left(-\int dz\{2m[V(z)-E]\}^{1/2}/\hbar\right). \tag{3}$$

It is important to notice that the decay rate of Eq. (3) is valid only at sufficiently large distances from the QW. Transition to the no-scattering limit is described by a pre-exponential factor, which depends on the specific scattering mechanism. The weakness of the scattering mechanisms leads to a small pre-exponential correction factor for the unperturbed wave function and essentially affects the distance from the QW where Eq. (3) can be used.[27] Experimental observations in the strong scattering regime confirm that lateral momentum in the exponential decay of the wave function is not conserved.[28] In the case of weak scattering, Meshkov's argument is valid further away from the QW and thus it does not affect measurable physical quantities.[27] This situation is shown in Fig. 2.

For the calculation of the thermionic current and the heat flux transported by electrons, we study the two limiting cases: no-scattering and strong momentum scattering.

III. CONSERVED LATERAL MOMENTUM CASE

In this case, the longitudinal (z) component of the wave function can be separated from the other degrees of freedom, and the lateral momentum is conserved. One can use Eq. (1) with a two dimensional density of states when the Fermi level is deep inside the well—similar to the case of quantum well photodetectors. However, the Fermi level in heterostructure thermionic coolers is close to the top of the barrier and one needs to consider the contribution of the electronic states above the barrier in the calculation of thermionic current. Figure 3(a) shows a schematic energy diagram for two neighboring wells. E_1 and E_2 are two quantized energy levels, E_f is the Fermi level, and E_b is the barrier height. Figure 3(b) shows k_1, k_2, k_f, and k_b, which are the wave vectors corresponding to the latter energies $(E_i=\hbar^2 k_i^2/2m)$.

Since states with $k_z>k_b$ are not confined in the QW, one cannot use a two dimensional density of states for them. The number of electrons that participate in thermionic emission process can be written directly as an integral in $k_x k_y k_z$ space

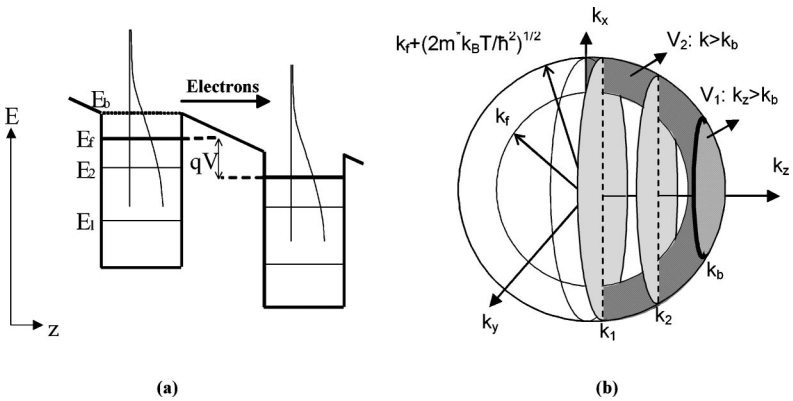

FIG. 3. (a) Conduction band and energy levels of two neighboring wells; (b) corresponding wave vectors in the k space: k_1, k_2, and k_b correspond to cross sectional planes and k_f is the radius of the Fermi sphere. V_1 is the volume of the electrons that participate in thermionic emission above the barrier if the lateral momentum is conserved. V_2 is that volume if the lateral momentum is not conserved.

$$n_e(V)=\frac{1}{L_w}\frac{1}{\pi^2}\sum_{k_{z_i}}\int_{-\infty}^{\infty}dk_x\int_{-\infty}^{\infty}dk_y[f(k_x,k_y,k_{z_i},E_f)-f(k_x,k_y,k_{z_i},E_f-qV)]T(k_{z_i},V)$$
$$+\frac{1}{2\pi^3}\left[\frac{L_w}{L_p}\int_{k_b}^{\infty}dk_z\frac{\hbar^2k_z^2}{m_w^*}\int_{-\infty}^{\infty}dk_x\int_{-\infty}^{\infty}dk_y\left(-\frac{\partial f(k_x,k_y,k_z,E_f)}{\partial E}\right)T(k_x,k_y,k_z,V)\right.$$
$$\left.+\frac{L_b}{L_p}\int_{0}^{\infty}dk_z\frac{\hbar^2k_z^2}{m_b^*}\int_{-\infty}^{\infty}dk_x\int_{-\infty}^{\infty}dk_y\left(-\frac{\partial f(k_x,k_y,k_z,E_f-E_b)}{\partial E}\right)T(k_x,k_y,k_z,V)\right], \tag{4}$$

where V is the applied voltage. The first integral gives the contribution to the transmitted electrons from the quantized energy levels of the well, corresponding to planes k_1, and k_2 in Fig. 3(b). The transmission probability, T, depends only on the V, and k_{z_i} value since we have assumed that the lateral momentum is conserved. The second and third integrals are the number of transmitted electrons from the energy band above the barrier located at the well and barrier regions respectively, corresponding to the states in volume V_1 in Fig. 3(b). The later two integrals are different in their reference of energy and the carrier's effective mass. For electrons in three-dimensional (3D) states above the barrier, we have used a bulk-type Boltzmann transport equation with a Fermi window factor of $(-\partial f/\partial E)$ and a correction due to the quantum mechanical transmission through the barrier. Equation (4) can be simplified by letting $k_{xy}\equiv\sqrt{k_x^2+k_y^2}$

$$n_e(V)=\frac{1}{L_w}\frac{2}{\pi}\sum_{k_{z_i}}\int_{0}^{\infty}dk_{xy}k_{xy}[f(k_{xy},k_{z_i},E_f)-f(k_{xy},k_{z_i},E_f-qV)]T(k_{z_i},V)+\frac{\hbar^2}{\pi^2}\left[\frac{L_w}{L_p}\int_{k_b}^{\infty}dk_z\frac{k_z^2}{m_w^*}\int_{0}^{\infty}dk_{xy}k_{xy}\right.$$
$$\left.\times\left(-\frac{\partial f(k_{xy},k_z,E_f)}{\partial E}\right)T(k_{xy},k_z,V)+\frac{L_b}{L_p}\int_{0}^{\infty}dk_z\frac{k_z^2}{m_b^*}\int_{0}^{\infty}dk_{xy}k_{xy}\left(-\frac{\partial f(k_{xy},k_z,E_f-E_b)}{\partial E}\right)T(k_{xy},k_z,V)\right]. \tag{5}$$

To calculate the thermionic figure-of-merit, one needs to obtain the energy transported by the electrons. We shall use the following quantity when calculating the thermionic cooling power Q

$$n_Q(V)=\frac{1}{L_w}\frac{2}{\pi}\sum_{k_{z_i}}\int_{0}^{\infty}dk_{xy}k_{xy}\frac{\hbar^2}{2m_w^*}(k_{xy}^2+k_{z_i}^2-k_f^2)[f(k_{xy},k_{z_i},E_f)-f(k_{xy},k_{z_i},E_f-qV)]T(k_{z_i},V)$$
$$+\frac{\hbar^2}{\pi^2}\left[\frac{L_w}{L_p}\int_{k_b}^{\infty}dk_z\int_{0}^{\infty}dk_{xy}k_{xy}\frac{k_z^2}{m_w^*}\frac{\hbar^2}{2m_w^*}(k_{xy}^2+k_z^2-k_F^2)\left(-\frac{\partial f(k_{xy},k_z,E_f)}{\partial E}\right)T(k_z,V)\right.$$
$$\left.+\frac{L_b}{L_p}\int_{k_b}^{\infty}dk_z\int_{0}^{\infty}dk_{xy}k_{xy}\frac{k_z^2}{m_b^*}\frac{\hbar^2}{2m_b^*}(k_{xy}^2+k_z^2-k_F^2+k_b^2)\left(-\frac{\partial f(k_{xy},k_z,E_f-E_b)}{\partial E}\right)T(k_z,V)\right]. \tag{6}$$

This equation is similar to Eq. (5) except that the integrand is multiplied by difference of the energy of emitted electrons from the Fermi level. We will use the above equations to calculate the thermionic current from: $I=qn_e(V)\nu A$, and the thermionic cooling power from: $Q=n_q\nu A$. A is the area of the microcooler, and ν is the electron drift velocity given by: $\nu=\mu F/\sqrt{1+(\mu F/\nu_s)^2}$, where μ is the mobility, ν_s is the saturation velocity, and F is the electric field in the barrier.

TABLE I. Structure parameters for the InGaAs/InAlAs superlattice cooler under study.

	n_w	L_w (nm)	L_b (nm)	V_b (meV)	m_{eff} (well/barrier)	β (W/mK)	μ ($\text{cm}^2/\text{V s}$)	v_s (cm/s)	α (eV^{-1})
$In_xGa_{1-x}As/In_xAl_{1-x}As$	50	30	10	500	0.041/0.07	5	6300–750	2×10^7	1.167

IV. NONCONSERVED LATERAL MOMENTUM

Interaction of the quantized charge carriers in the quantum well, both with each other and with inhomogeneities, couples the in-plane and the perpendicular-to-the-plane degrees of freedom. Thus, lateral momentum may not be conserved during thermionic emissions, and in this case the transmission probability depends on the total energy of the electron, and not just the kinetic energy perpendicular to the well.[19,26,29] One thus replaces $T(k_z,V)$ with $T(k_{xy},k_z,V)$ in the first term of Eqs. (4), (5), and (6), and the states with $k>k_b$ will participate in transport (as shown in Fig. 3)

$$n_e(V)=\frac{1}{L_w}\frac{2}{\pi}\sum_{k_{z_i}}\int_0^\infty dk_{xy}k_{xy}[f(k_{xy},k_{z_i},E_f)-f(k_{xy},k_{z_i},E_f-qV)]T(k_{xy},k_{z_i},V)+\frac{\hbar^2}{\pi^2}\left[\frac{L_w}{L_p}\iint\limits_{k_{xy}^2+k_z^2>k_b^2}dk_{xy}dk_z \times k_{xy}\frac{k_z^2}{m_w^*}\left(-\frac{\partial f(k_{xy},k_z,E_f)}{\partial E}\right)T(k_{xy},k_z,V)+\frac{L_b}{L_p}\iint\limits_{k_{xy}^2+k_z^2>0}dk_{xy}dk_zk_{xy}\frac{k_z^2}{m_b^*}\left(-\frac{\partial f(k_{xy},k_z,E_f-E_b)}{\partial E}\right)T(k_{xy},k_z,V)\right]. \tag{7}$$

For the thermionic cooling power Q, the following integral is used:

$$n_Q(V)=\frac{1}{L_w}\frac{\hbar^2}{\pi m_w^*}\sum_{k_{z_i}}\int_0^\infty dk_{xy}k_{xy}(k_{xy}^2+k_{z_i}^2-k_f^2)[f(k_{xy},k_{z_i},E_f)-f(k_{xy},k_{z_i},E_f-qV)]T(k_x,k_y,k_{z_i},V) +\frac{\hbar^4}{2\pi^2}\left[\frac{L_w}{L_p}\iint\limits_{k_{xy}^2+k_z^2>k_b^2}dk_{xy}dk_zk_{xy}\frac{k_z^2}{m_w^{*2}}(k_{xy}^2+k_z^2-k_F^2)\left(-\frac{\partial f(k_{xy},k_z,E_f)}{\partial E}\right)T(k_{xy},k_z,V) +\frac{L_b}{L_p}\iint\limits_{k_{xy}^2+k_z^2>0}dk_{xy}dk_zk_{xy}\frac{k_z^2}{m_b^{*2}}(k_{xy}^2+k_z^2-k_F^2+k_b^2)\left(-\frac{\partial f(k_{xy},k_z,E_f-E_b)}{\partial E}\right)T(k_{xy},k_z,V)\right]. \tag{8}$$

V. InGaAs BASED SUPERLATTICES

In this section, we will study the thermionic cooling efficiency in heterostructures. We will specifically examine two cases: conserved and nonconserved lateral momentum. For practical purposes a superlattice of InGaAs/InAlAs is chosen for this study. An InGaAs/InAlAs superlattice is interesting for long wavelength laser applications where an integrated on-chip cooler could be quite useful. A superlattice thermionic cooler made of HgCdTe is also studied for a comparison of performance which could outperform the current commercial thermoelectric coolers. Material parameters that we have taken for these two structures are tabulated in Tables I and II.

n_w is the number of wells. L_w and L_b are well and barrier widths, respectively. V_b is the barrier height. β, μ, α, and V_s are thermal conductivity, mobility, nonparabolicity coefficient, and the saturation velocity, respectively. Mobility depends on the doping concentration. Experimental measurements have been fit with the following equation in the range of practical dopings: $\mu=37666-1845.61\times\log_{10}(n_e)$ in unit of $\text{cm}^2/\text{V s}$, where n_e is the bulk doping concentration in cm^{-3}. We have used this mobility in all simulations for InGaAs/InAlAs materials. Superlattice structures presented in this article have a doped well region and undoped barriers. However, we are using the mobility related to the doped region, which is a worst-case estimate for the mobility of the

TABLE II. Structure parameters for the HgCdTe superlattice cooler under study.

	n_w	L_w (nm)	L_b (nm)	V_b (meV)	m_{eff} (well/barrier)	β (W/mK)	μ_w/μ_b ($\text{cm}^2/\text{V s}$)	v_s (cm/s)
$Hg_{0.8}Cd_{0.2}Te/Hg_{0.2}Cd_{0.8}Te$	50	30	10	730	0.012/0.069	0.97	10 000/191	5×10^7

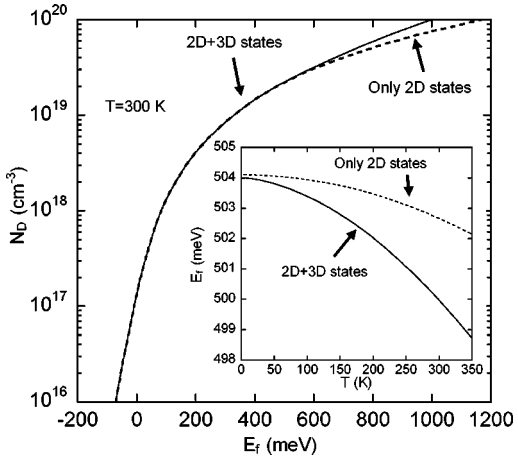

FIG. 4. Fermi energy vs doping at 300 K and vs temperature at $N_D = 2.26\times10^{19}\,\mathrm{cm}^{-3}$ (see inset) for the proposed InGaAs/InAlAs structure of Table I. Dotted curve considers only the 2D quantized states of the quantum wells, and solid curve includes 3D states of above the barrier as well.

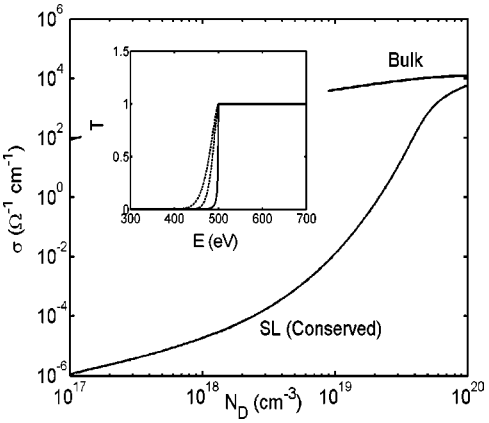

FIG. 5. Conductivity of InGaAs bulk and InGaAs/InAlAs vs doping when the lateral momentum is conserved. Inset shows the calculated transmission probability vs energy using Wentzel–Kramers–Brillouin (WKB) approximation where solid and dotted curves correspond to applied electric fields of 1, 12.5, and 25 kV/cm, respectively. The applied electric filed in the present calculations of thermoelectric properties is assumed to be 1 kV/cm.

whole structure. Since the barrier region is undoped, a higher mobility for electrons is expected.

To achieve the desired performance of thermionic coolers, several factors have key contributions. In particular, as discussed in Refs. 1, 2, and 6 the Fermi energy must be carefully chosen to create an asymmetric energy distribution of electrons moving in the material with respect to the Fermi energy—giving a higher Seebeck coefficient while reducing the Joule heating that resulted from the conductivity reduction in the superlattices compared to that of bulk material. It turns out that for this purpose, the Fermi level should be located a few thermal energy below the barrier height. As a result, the 3D states above the barrier dominate the effect of the two-dimensional states in the well. Considering that, the 3D states will affect the position of Fermi level as well as number of electrons contributing to the thermionic emission. Equations (4)–(8) explain in detail how the states above the barrier and their energy transfer can be taken into account. The Fermi level can be calculated from the following expression for the carrier concentration in the material:

$$N_D = \frac{1}{L_W}\sum_i \int_0^\infty dk_{xy}\frac{k_{xy}}{\pi} f(k_{xy},k_{z_i},E_f) + 2\int_0^\infty dk_{xy}\int_{k_b}^\infty dk_z \frac{k}{2\pi^2} f(k_{xy},k_z,E_f) + \frac{2L_b}{L_W}\int_0^\infty dk_{xy}\int_0^\infty dk_z \frac{k}{2\pi^2} f(k_{xy},k_z,E_f-E_b). \quad (9)$$

The first integral gives the number of electrons confined in the well and the second and third integrals are the electrons in 3D states above the barrier in the well and barrier region, respectively. The $1/L_W$ factor in the first term is used to transform the 2D density of states to the 3D doping in the well. Since only the well regions are doped, the L_b/L_W factor is placed in front of the second integral to consider the nonuniform doping, and m_w^* and m_b^* are the effective masses of electron in the well and barrier regions, respectively.

One should notice that since the regions in Fig. 3(b) could not be easily described in spherical coordinates, these

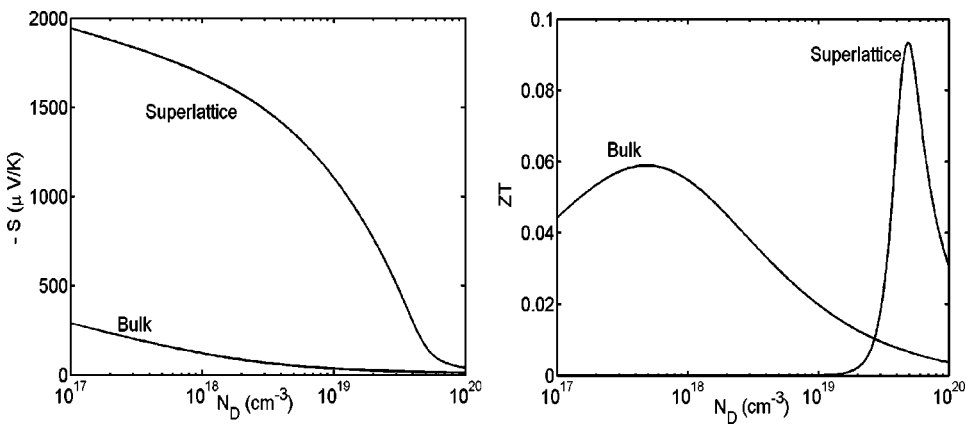

FIG. 6. Seebeck coefficient (left) and coefficient of performance (ZT) vs doping for InGaAs bulk and InGaAs/InAlAs superlattice.

integrals and the ones in Eqs. (4)–(6) should be written in terms of a wave vector of the electron (k) rather than the energy (E).

Figure 4 shows the Fermi energy versus doping for the structure of InGaAs/InAlAs superlattice. There are ten quantized energy levels for each well whose three last ones are $E_n = 250.7$, 301.8, and 347.5 meV. A dashed curve is for the case if the presence of 3D states above the barrier is not taken into account. The data shows that 3D states play a significant role in determining the Fermi energy at high doping densities.

Let us now calculate the current–voltage ($I-V$) and the cooling characteristics of this superlattice structure in the two limiting cases of conserved and nonconserved lateral momentum. For the conserved lateral momentum case, we will use Eqs. (4) and (6), calculating the thermionic current from: $I = qn_e(V)\nu A$, and the thermionic cooling power from: $Q = n_q \nu A$. A is the area of the micro cooler, and ν is the electron drift velocity given by: $\nu = \mu F/\sqrt{1+(\mu F/\nu_s)^2}$ where μ is the mobility, ν_s is the saturation velocity, and F is the electric field in the barrier. One should note that since wells are heavily doped and barriers are undoped, almost all of the potential drop would be in the barrier region. Effective conductivity σ can be calculated from $I-V$ according to: $\sigma = IL_p n_w/AV$, where L_p is the period of the superlattice and n_w is the number of wells. In an analogy with thermoelectrics, one can define the thermionic figure-of-merit, also known as coefficient of performance (COP) as: $ZT = \sigma S^2 T/\beta$, where β is the thermal conductivity of the material and S is the effective Seebeck coefficient, which can be calculated from Q and I according to: $S = Q/IT$.

Figure 5 shows the calculated electrical conductivity for InGaAs bulk and InGaAs/InAlAs superlattices when the lateral momentum is conserved. Material parameters are taken from Table I. The conductivity of the superlattice is reduced due to the selective emission of electrons over the barrier. This structure is intentionally chosen to compare the model presented here with previous results on thermionic cooling performance.[30–32] It has been shown that the figure-of-merit for thermionic cooling is about half of that of thermoelectric cooling in InGaAs. In Fig. 6 the corresponding Seebeck coefficient (left) and the figure-of-merit (right) are presented. Although the Seebeck coefficient is higher in superlattice structures, the figure-of-merit remains about the same as it is in bulk InGaAs. This is again due to the conductivity reduction in the superlattice structure. This result is similar to the one previously studied on thermionic/thermoelectric refrigeration.[16] However, there are several assumptions made in order to reach this result. Thermionic current has contributions from both 2D and 3D states of the well that have energies above the barrier. The superlattice structure chosen here has wide wells with several quantized states that reduce the effect of 3D states on thermionic current. A more important assumption is that the lateral momentum of electrons is conserved. As we will see, violation of this assumption can make a significant difference in both conductivity and ZT. While models similar to that in Ref. 16 do not converge to bulk when the barrier height (E_b) is reduced to zero, our model has this advantage: when E_b goes to zero, ZT of superlattice converges to that of bulk.

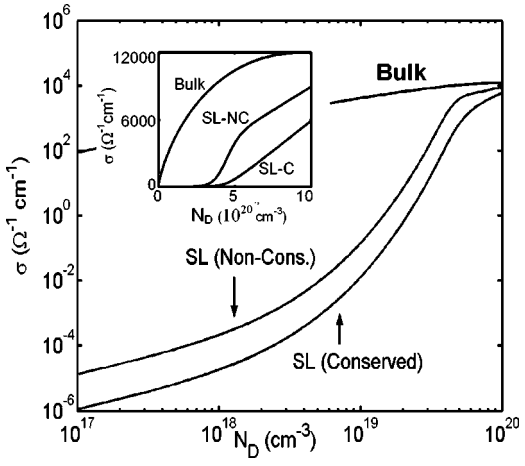

FIG. 7. Effective conductivity vs doping for InGaAs bulk, and superlattice assuming conserved and nonconserved lateral momentum for the structure of Table I.

As we explained in Sec. II, nonconservation of lateral momentum can increase the number of electrons participating in a thermionic current. This can significantly improve the cooling power of HIT coolers. We use Eqs. (7) and (8) to calculate the thermionic current and the corresponding cooling power density. Figure 7 shows the calculated conductivity versus doping assuming that lateral momentum of the electrons is not conserved during transport. For comparison

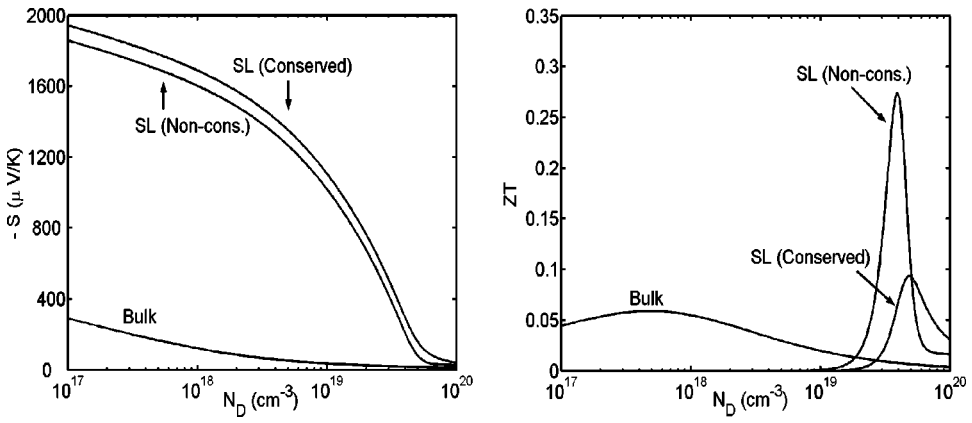

FIG. 8. Seebeck coefficient (left) and ZT (right) vs doping for InGaAs bulk, and superlattice assuming conserved and nonconserved lateral momentum for the structure of Table I.

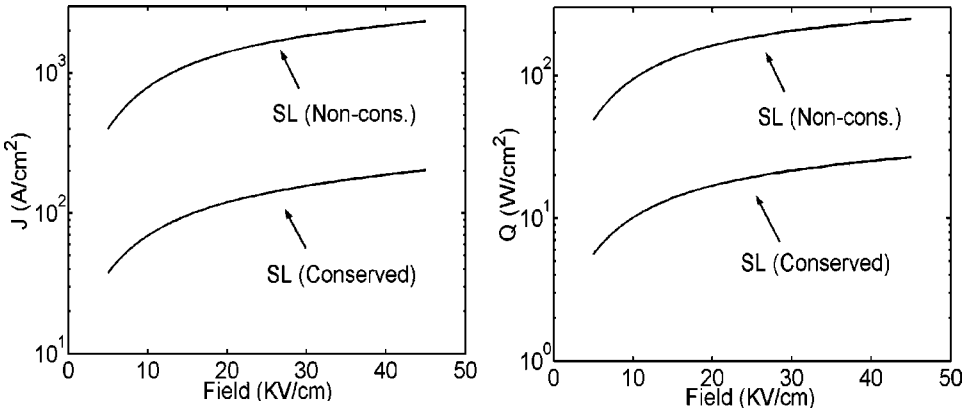

FIG. 9. Current density (left) and cooling power density (right) vs applied electric filed for InGaAs superlattice structure of Table I for the two cases of conserved and nonconserved lateral momentum.

we have plotted conductivity of bulk material and superlattice if the lateral momentum remains conserved. It can be seen that at low doping, when the Fermi energy lies deep in the well, the conductivity of the superlattice is several orders of magnitude less than that of the bulk. However, as the doping increases 3D states above the barrier participate more in thermionic current and conductivity increases accordingly. When the Fermi energy approaches the barrier edge, the conductivity of the superlattice is almost equal to that of the bulk. In Fig. 7 there is still a small difference between the conductivity of the superlattice and that of the bulk at a high doping concentration, which is due to the modulation doping of superlattice where only the well regions are doped. Therefore the superlattice structure has an effective doping on the order of L_w/L_p less than that of a uniformly doped bulk.

Figure 8 plots the corresponding calculated Seebeck coefficient (S) and the coefficient of performance (ZT). It can be seen that Seebeck coefficient is significantly increased in the superlattice structure when compared to that in bulk. In this case the ZT is about six times larger than that in the bulk material.

One should note that as we are in nonlinear transport regime, the effective conductivity and COP are voltage dependent. They depend on the voltage of the electric field applied over the superlattice. Figure 9 shows the electric field's dependence on the current density and the cooling power density.

Current density and cooling power density are plotted for the InGaAs superlattice structure described in Table I, with a doping concentration of $3\times10^{19}\,\mathrm{cm}^{-3}$ in the well. Plots labeled with SL (conserved) and SL (nonconserved) are for those cases where the lateral momentum is and is not conserved, respectively. It can be seen that the conductivity depends on the applied electric field. However, as both current density (J) and cooling power density (Q) change with the applied field in the same fashion, the Seebeck coefficient still remains constant over the range of the applied field. The change of conductivity with the applied filed does change, however, the coefficient of performance (ZT) accordingly. Figure 10 shows how conductivity and ZT change over the range of applied electric field. Conductivity decreases with an applied electric field both in bulk materials and superlattices due to the electron velocity saturation. The coefficient of performance decreases when the electric field is increased accordingly.

VI. HgCdTe BASED SUPERLATTICES

In another example we have considered an HgCdTe superlattice cooler. Its structural parameters are listed in Table II. Although the effective mass in HgCdTe is less than that in InAlAs, there are two advantages in HgCdTe superlattice coolers that make it more attractive than InAlAs superlattice coolers. First, the thermal conductivity of HgCdTe is five times less than that of InAlAs. Second, it is possible to get higher barrier heights—as high as 730 meV.

In Fig. 11 we have plotted the conductivity of HgCdTe bulk and the considered HgCdTe superlattice for two cases of conserved and nonconserved electron lateral momentum.

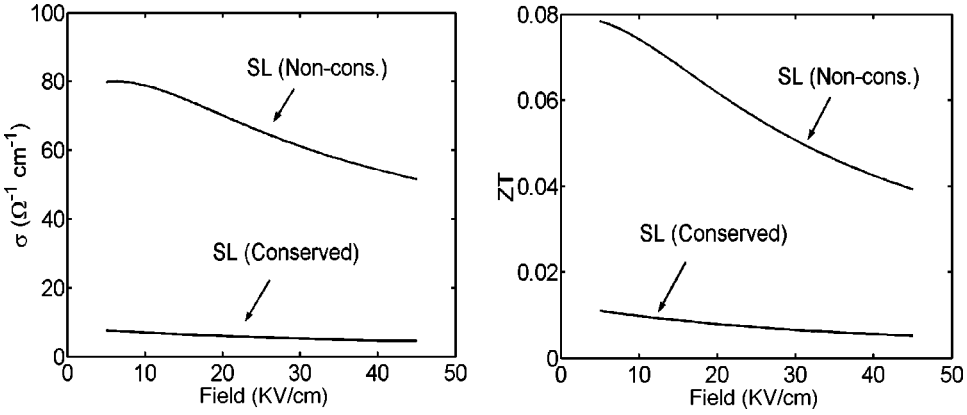

FIG. 10. Effective conductivity vs electric field assuming conserved and nonconserved lateral momentum for the structure of Table I (left) and the corresponding ZTs (right).

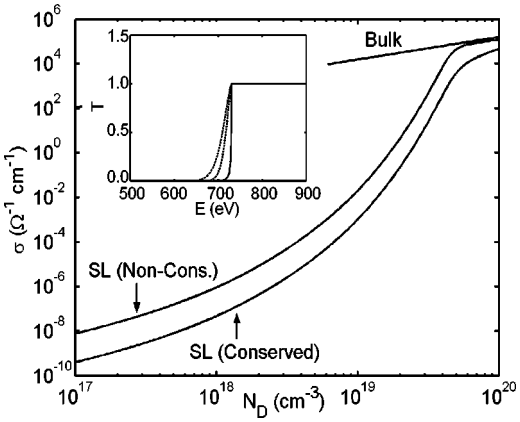

FIG. 11. Effective conductivity vs doping for HgCdTe bulk, and superlattice assuming conserved and nonconserved lateral momentum for the structure of Table II. Inset shows the calculated transmission probability vs energy using WKB approximation where solid and dotted curves correspond to applied electric fields of 1, 12.5, and 25 kV/cm, respectively. The applied electric field in the present calculations of thermoelectric properties is assumed to be 1 kV/cm.

Again, as it can be in Fig. 12, the nonconservation of lateral momentum significantly improves the performance of thermionic coolers. The higher ZT of HgCdTe compared to that of InAlAs is due to its lower thermal conductivity and higher barrier height. It is important to note that thermal conductivity is often reduced in superlattice structures. In order to isolate the cooling improvement due to the thermionic emission of electrons over the barrier, we are not considering the reduction in lattice thermal conductivity in our comparison of bulk and superlattice structures. Taking it into account would cause an even higher ZT in HgCdTe superlattices because ZT increases inversely with the reduction of thermal conductivity.

For a comparison with the model presented in Ref. 17 that takes into account the superlattice full band structure, we calculate the Seebeck coefficient and the figure of merit (ZT) for $Hg_{0.75}Cd_{0.25}Te$ alloy and 50 Å $Hg_{0.75}Cd_{0.25}Te$/140 Å $Hg_{0.8}Cd_{0.3}Te$ superlattice for the structure presented in Ref. 17. Mobility is taken equal to 7500 $cm^2/V\,s$ with an effective mass of $0.018m_e$ for the electrons. In Ref. 17 mobility is calculated at each density. Although this can change the absolute value of the calculated quantities, the trend of improved performance for the superlattice structure and the continuing role of nonconservation of lateral momentum should be still correct. The thermal conductivity of the bulk material is 9.7 mW/cm K and we are assuming that the thermal conductivity of superlattice is a factor of 10 smaller than its magnitude in the bulk material according to Ref. 17. This is the only place that we are assuming a different thermal conductivity for the superlattice in the calculations of this article. Barrier height is taken to be 55 meV, and the calculations are done for the room temperature (300 K). Figure 13 shows the calculated Seebeck coefficient and ZT. Optimum values are tabulated in Table III.

As before, SL (conserved) and SL (nonconserved) correspond to the cases where the conservation of lateral momentum is and is not conserved, respectively. Although the absolute values are different from that of Ref. 17 because of the simplifications of energy dependency of the mobility and the band structure, the trend remains the same. Superlattice structure has an improved ZT compared to its magnitude in bulk, which is only due to the assumed, reduced, thermal conductivity of the superlattice. Although the thermal conductivity of the superlattice is taken to be ten times smaller than that of the bulk, this improvement is less than a factor of 10 in both calculations of the model presented here and in Ref. 17. This means that the superlattice transport is degrading the cooling performance of the structure. A significant improvement cannot be seen for the case where lateral momentum is not conserved. This is due to small barrier heights in the superlattice. We saw in a previous section that with a large barrier height, a significantly higher ZT can be achieved with a proper doping concentration in the superlattice structure.

VII. ASYMMETRIC BARRIER

Another factor that could influence the performance of HIT coolers is the nonsymmetric barrier between the cathode and anode. Let us consider a single barrier device. A thermionic emission's current density is proportional to the difference between the number of filled initial states and empty, or available, final states: $f(E,E_f)\times(1-f(E,E_f-qV))$, where V is the voltage across the barrier. One should also consider the reverse current. Thus the total current is proportional to

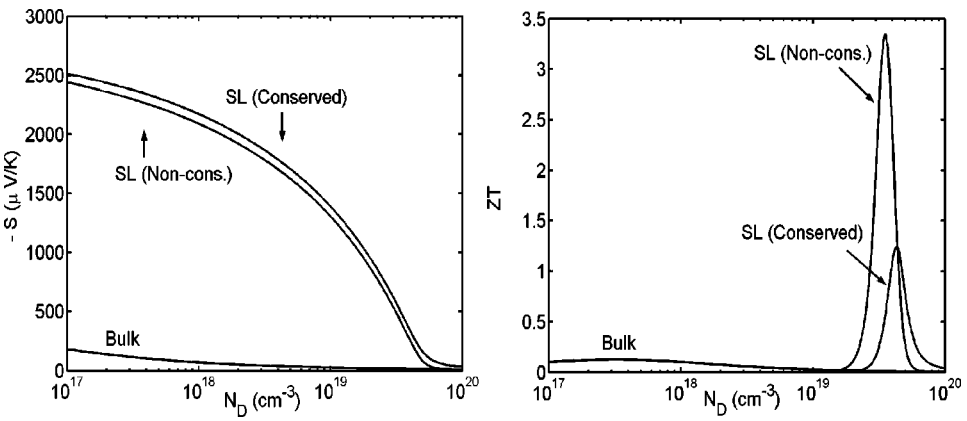

FIG. 12. Seebeck coefficient (left) and ZT (right) vs doping for HgCdTe bulk, and superlattice assuming conserved and nonconserved lateral momentum for the structure of Table II.

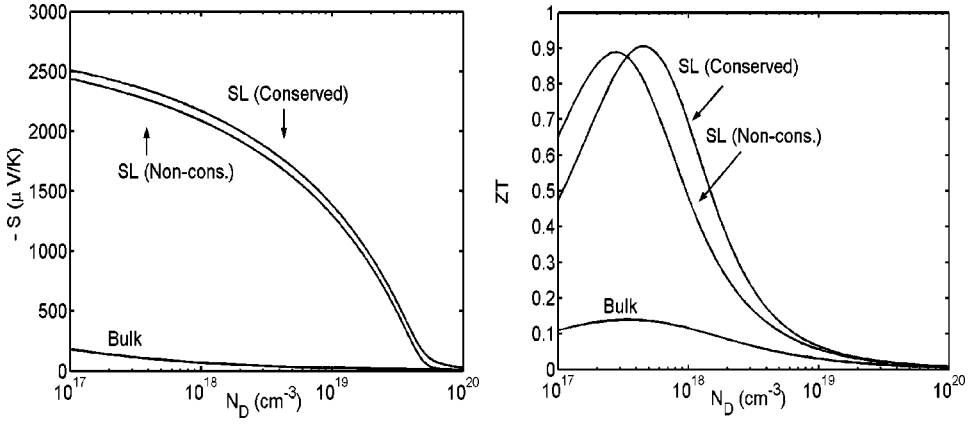

FIG. 13. Seebeck coefficient (left) and ZT (right) vs doping $Hg_{0.75}Cd_{0.25}Te$ bulk, and $Hg_{0.75}Cd_{0.25}Te/Hg_{0.8}Cd_{0.3}Te$ superlattice assuming conserved and nonconserved lateral momentum.

$$J(E) \propto f(E,E_f) \times (1-f(E,E_f-qV)) - f(E,E_f-qV) \times (1-f(E,E_f)) = f(E,E_f) - f(E,E_f-qV). \quad (10)$$

This term appears in Eq. (1) as well as subsequent equations. The above factor in the transport equation should only be used for symmetric barriers. The second term in Eq. (10) reduces the current density significantly.

In the case of an asymmetric barrier, where the reverse current is reduced, the cooling power density can be significantly enhanced.

Notice that the increased cooling power is achieved at the expense of lower efficiency. Compared to the symmetric barrier at anode and cathode sides, larger voltages are needed to achieve the same electric field in the barrier region. This creates an increased heating in the anode side and lowers the refrigeration efficiency.

For comparison we have calculated and plotted the cooling power density versus applied electric field for the InGaAs/InAlAs superlattice of Table I in Fig. 14. The barrier is undoped and the well is doped to $5\times10^{18}\,\mathrm{cm}^{-3}$. The lateral momentum of electrons is assumed to be conserved here. The cooling power density is about 3.7 times larger in an asymmetric barrier than in a symmetric barrier at low electric fields.

VIII. METALLIC SUPERLATTICE

Metals have a large number of electrons participating in the conduction process; furthermore they have very large electrical conductivities. However, metals tend to have very low Seebeck coefficients which results in low thermoelectric figures of merit (ZT). The low Seebeck coefficient is due to the fact that when the Fermi energy is deep inside the conduction band, the contribution of electrons with different energies to the conduction process (differential conductivity) is symmetric with respect to the Fermi energy [Fig. 15 (middle)]. An introduction of tall barriers inside metal will allow the filtering of hot electrons and thus the Seebeck coefficient can be significantly increased [Fig. 15 (right)].

This is shown pictorially by plotting the differential conductivity in Fig. 15. A maximum ZT of an InAlAs alloy happens at doping concentrations of 3.5×10^{17} which correspond to a Fermi energy equal to 28.6 meV above the conduction band edge. Figure 15 (left) shows its nonsymmetric distribution of electrons compared to the Fermi energy. While the Seebeck coefficient is relatively high, the number of conduction electrons is small; additionally conductivity is low resulting in low ZT of 0.054. In metals the number of conduction electrons is high, but they are symmetrically distributed around the Fermi energy [Fig. 15 (middle)]. Figure 15 (right) shows the differential conductivity of a metallic superlattice with a Fermi energy of 10.81 eV and barrier height of 10.93 eV, which results in a high ZT of 6.8. This is due to the higher electrical conductivity and a Seebeck coefficient that resulted from the asymmetric distribution of transported electrons compared to Fermi energy. Mobility is taken to be 12.2 $\mathrm{cm}^2/\mathrm{V\,s}$, the value for a typical metal. Thermal conductivity in metals is dominated by electron thermal conductivity that is approximately $2.44\times10^{-8}\,\sigma T$ in units of W/K according to the Wiedemann–Franz law. However, electrical conductivity (σ) in a metallic superlattice is low compared to that in bulk metal, and hence electron thermal conductivity can be comparable to that of phonons in the barrier. Therefore, ZT is also dominated by the thermal conductivity of the barrier layer. We are assuming a barrier thermal conductivity of 1 W/mK for these calculations. Figure 16 shows the calculated thermoelectric figure-of-merit for a metallic superlattice versus Fermi energy. The optimum barrier height for maximum ZT is shown on the right axis. One

TABLE III. Optimum values for ZT, S, and N_D.

	Bulk	SL (Conserved)	SL (Nonconserved)	Bulk[a]	SL[a]
S_{opt} (μV/K)	−125	−235	−238	−224	−291
ZT_{opt}	0.14	0.9	0.89	0.5	1.7
$(N_D)_{opt}$ (cm^{-3})	3.5×10^{17}	4.6×10^{17}	2.8×10^{17}	2.7×10^{17}	1.4×10^{17}

[a]See Ref. 17.

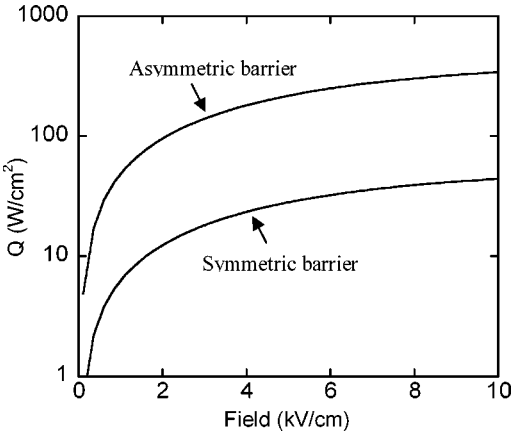

FIG. 14. Cooling power density for an asymmetric (dotted) and asymmetric InGaAs/InAlAs superlattice.

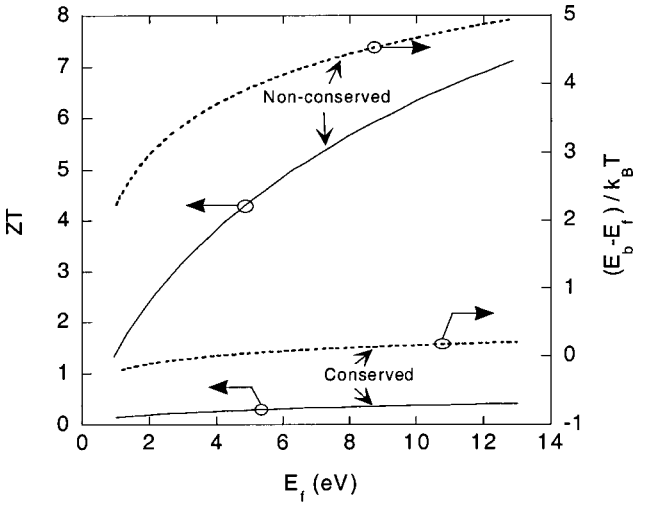

FIG. 16. Thermoelectric figure of merit (left axis) and optimum barrier height (right axis) vs Fermi energy for a metallic superlattice.

should notice that the conservation of lateral momentum plays an important role in determining the number of carriers that participate in the conduction process in metallic superlattices. Its significant influence on ZT is noticeable in Fig. 16. While the ZT for the case of conserved lateral momentum remains less than 1 in this superlattice structure, it increases to about 7 for the case of nonconserved lateral momentum.

Moyzhes and Nemchinsky[14] have mentioned the use of nonplanar interfaces in order to reduce metal/semiconductor electrical boundary resistances by increasing the effective area between the two layers. One should consider, however, that the geometric argument for increased surface area does not take into account the length scale necessary to achieve nonconservation of lateral momentum. If the surface roughness is smaller than an electron's de Broglie wavelength, the electron wave sees only an effective interface layer and this does not affect lateral momentum conservation. In the limit of large roughness ($\geqslant$electron mean-free-path) current flow through the interface could become nonuniform. In order to achieve nonconservation of lateral momentum, a nonplanar interface with a roughness bigger than the electron's de Broglie wavelength and smaller than the electron's mean-free-path is necessary. This can be achieved using embedded quantum dot structures (see for example Refs. 33 and 34).

In the Appendix, the current–voltage characteristics of a variety of superlattice structures are analyzed and the results are compared with the experimental data. We show how the assumption that lateral momentum is conserved can explain the observed data in a wide range of temperatures in semiconductor superlattices with planar interfaces. This is in contrast with Refs. 19 and 30 which had to assume nonconservation of lateral momentum in order to explain dark current in GaAs/InAlAs QWIPs. The key difference is in the inclusion of 3D states above the barrier, which allows fitting the experimental $I-V$ results to a variety of superlattice structures.

In the case of metal/semiconductor barriers, detailed experimental results were obtained by using ballistic electron emission microscopy by Narayanamurti *et al.*[35] These have shown that nonplanar interfaces give rise to significant current increase due to nonconservation of lateral momentum. Additionally, detailed theoretical calculations by Smith *et al.*[36,37] shows that a significant number of electrons going across the barrier do not obey conservation of lateral momentum.

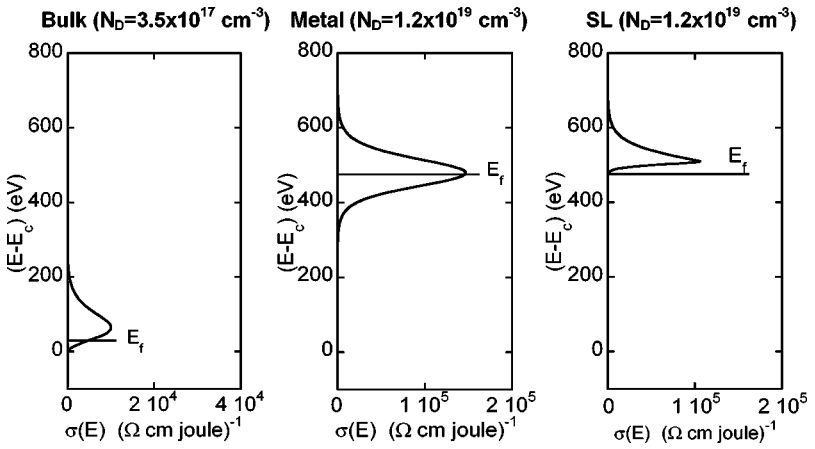

FIG. 15. Differential conductivity for AlGaAs alloy (left) regular metal (middle) and for metallic superlattices (right).

TABLE IV. Quantum well parameters of the QWIPs: L_w, well width; L_b barrier width; N_D, doping density in the well; and V_b, barrier height.

Reference	N_D (cm^{-2})	x	n_w	L_w (nm)	L_b (nm)	V_b (meV)
19	4×10^{11}	0.29	50	4	30.5	247
42	1.5×10^{11}*	0.267	41	5.5	34.6	227
43	2.5×10^{10}	0.15	50	5	50	127.2

*Only 1/3 central part of the well is doped.

IX. CONCLUSION

We have presented a detailed calculation of thermionic current and electronic heat transport in semiconductor and metallic superlattice structures. We studied two limiting cases to determine the number of electrons participating in a thermionic emission process that is based on the conservation of lateral momentum. Nonplanar barriers or scattering can mix the planar motion of the carriers with the longitudinal motion (perpendicular to the barrier) and remove the requirement for the conservation of lateral momentum. Therefore, in the latter case, the transmission probability depends not only on the perpendicular component to the barrier, but also on the total kinetic energy of the electrons. This will dramatically increase the number of electrons that are transmitted over the barrier. These electrons are responsible for thermionic cooling, and thereby thermionic cooling power is increased. The conservation of lateral momentum is a consequence of translational invariance in the plane of QW. It is possible by introducing controlled roughness at interface to break this translational invariance and increase the thermionic cooling power density. It is important to note that the roughness can also decrease the electron mobility in the material and increase Joule heating. However experimental results with GaAs/InAlAs QWIPs show that it is possible to have large mobility for carriers moving above the barrier (see Appendix). By controlling the roughness of the superlattice interfaces during the growth or by taking advantage of well designed quantum dot structures the required inhomogeneities can be created.[38] The improvement in the effective power factor through thermionic emission can be combined with the other methods to reduce the phonon thermal conductivity in superlattices and thus obtain a higher thermoelectric cooling power factor.[39–41]

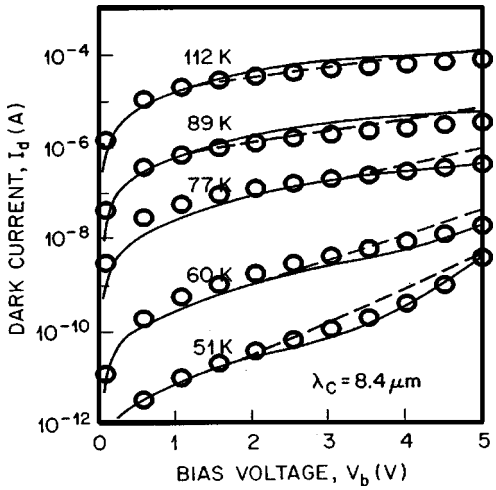

FIG. 17. Experimental (solid curves) and theoretical (dashed) dark current–voltage characteristics curves at various temperatures from Ref. 19. Circled curves are the result of the calculations for the same structure using the model presented in this article with the assumption that the lateral momentum for transported electrons is conserved.

ACKNOWLEDGMENTS

This work was supported by the Packard Foundation and the ONR MURI on Thermionics.

APPENDIX: COMPARISON WITH EXPERIMENTAL DATA

The model presented can be verified using the data available for dark current in QWIPs. We hereby present a comparison with three experimental data from Refs. 19, 42, and 43. In our calculations we are using the same parameters used in these references for fitting the experimental data. Samples are all grown by molecular beam epitaxy on semi-insulating GaAs substrate. The period of superlattice structure consists of a GaAs well and $Al_xGa_{1-x}As$ barriers. The GaAs well region is doped with Si. Quantum well parameters used in the calculations are listed in Table IV.

Dark current for detectors of Ref. 19 is calculated and plotted in Fig. 17 as a function of voltage and temperature and is compared with the measurement data given in Ref. 19. This structure, with 200 μm diameter, consists of a 50-period multiquantum well superlattice having a well width L_w of 40

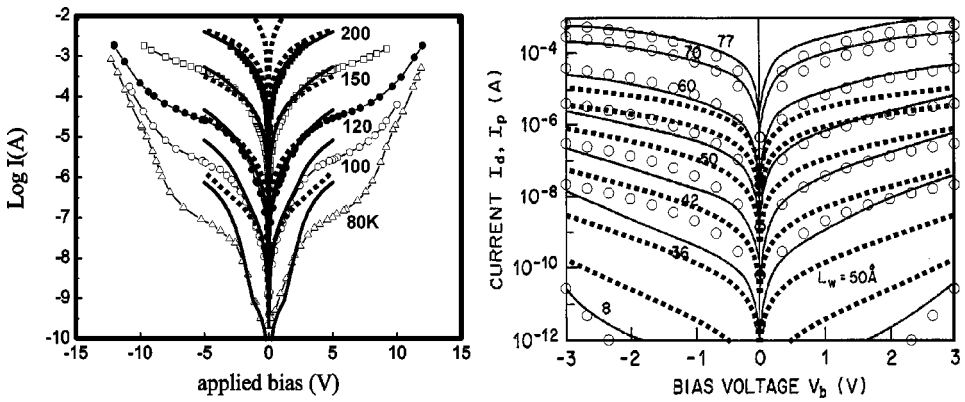

FIG. 18. Dark current bias voltage curves as a function of temperature for the samples of Refs. 42 (left) and 43 (right). In the left plot, curves with symbols are experimental curves, and dotted and solid curves are calculated using the model presented in Ref. 19 and in this article, respectively. In the right plot, solid curves are from experimental data, and dotted and circled curves are calculated using the model presented in Ref. 19 and in this article, respectively.

Å and a 305 Å barrier width with L_b of $Al_{0.29}Ga_{0.71}As$. As stated in Ref. 19, these parameters were varied within the experimental errors to optimize their theoretical fit. The values that they determined were $L_w = 38$ Å and $L_b = 320$ Å. However, in this simulation, L_w and L_b are taken to be the same as the given growth values. Other parameters are similar to those in Ref. 19. It is interesting to note that the model presented in Ref. 19 fits the experimental data very well when it is assumed that the lateral momentum of electrons is not conserved in superlattice transport. However, using the model presented in this article, a good agreement is also achieved as a function of both bias voltage and temperature over a range of 8 orders of magnitude in dark current.[44] The reason that the authors of Ref. 19 had to assume nonconservation of lateral momentum to fit the experimental data is that they were mainly neglecting the transport through the three dimensional states above the barrier. Thus, if they assumed conservation of lateral momentum, the calculated current would be too small to fit the experimental data.

Another factor that has been considered in the calculations of the dark currents is the barrier lowering due to the increasing of the electric field. As it is explained in Ref. 42, when increasing the applied electric field, the barrier height decreases due to both a geometrical effect and a situation similar to the Poole–Frenkel effect[45] but with taking into account of finite thickness of the electron trap (the QW thickness). This increases the number of 3D states close to top of the barrier that also increases the thermionic current. It is shown that the barrier is decreased by $\alpha F^{1/2}$, where F is the electric field and $\alpha = (e/\pi\epsilon\epsilon_0)^{1/2}$.[42] The value, e, is the charge of an electron and ϵ is the dielectric constant of the material.

For further verification of our model, we have calculated the current voltage characteristics of two other structures presented in Refs. 42 and 43 and plotted them in Fig. 18. We first used the model presented in Ref. 19 and plotted the curves for the detector with a mesa structure of 100×100 μm^2 given in Ref. 42. Dotted curves in Fig. 18 (left) show this result.[46] It can be seen that the current is orders of magnitude higher than what is found in the experimental data, which is shown by curves with symbols. Then we calculated the dark current using our model under the assumption that the lateral momentum of electrons is conserved. The result is shown with solid curves in Fig. 18 (left). It can be seen that at a low field region the calculations based on our model have an adequate fit to the experimental data for the whole range of temperatures. However, at higher fields (above 3 kV/cm at low temperature) the model's expectations diverge from experimental results. This is due to moving to high field transport regime and possible formation of nonuniform electric field domains in the device which is beyond the scope of this article.[47]

For another verification of our model, we calculated and plotted the current–voltage curves for the photodetectors (200 μm diameter) of Ref. 43. This is shown in Fig. 18 (right).

It can be seen that the model presented in Ref. 19, which is adopted in many other works (for example: Refs. 19–25), is again orders of magnitude higher than the experiment while the model presented here provides a closer fit with the data when the conservation of lateral momentum is conserved.[48]

Thus, while the model based on nonconservation of lateral momentum is not able to fit all of the curves for the whole range of applied fields, we are presenting a model which is able to match different experimental data with a good accuracy as a function of both bias voltage and temperature over a range of several orders of magnitude in dark current.

[1] A. Shakouri and J. E. Bowers, Appl. Phys. Lett. **71**, 1234 (1997).
[2] A. Shakouri, E. Y. Lee, D. L. Smith, V. Narayanamurti, and J. E. Bowers, Microscale Thermophys. Eng. **2**, 37 (1998).
[3] A. Shakouri, C. LaBounty, J. Piprek, P. Abraham, and J. E. Bowers, Appl. Phys. Lett. **74**, 88 (1999).
[4] A. Shakouri, C. Labounty, P. Abraham, J. Piprek, and J. E. Bowers, Mater. Res. Soc. Symp. Proc. **545**, 449 (1998).
[5] G. H. Zeng, A. Shakouri, C. La Bounty, G. Robinson, E. Croke, P. Abraham, X. F. Fan, H. Reese, and J. E. Bowers, Electron. Lett. **35**, 2146 (1999).
[6] X. F. Fan *et al.*, Appl. Phys. Lett. **78**, 1580 (2001).
[7] X. F. Fan, G. Zeng, E. Croke, C. LaBounty, C. C. Ahn, D. Vashaee, A. Shakouri, and J. E. Bowers, Electron. Lett. **37**, 126 (2001).
[8] C. LaBounty, A. Shakouri, P. Abraham, and J. E. Bowers, Opt. Eng. (Bellingham) **39**, 2847 (2000).
[9] C. LaBounty, A. Shakouri, and J. E. Bowers, J. Appl. Phys. **89**, 4059 (2001).
[10] T. F. Zeng and G. Chen, Microscale Thermophys. Eng. **4**, 39 (2000).
[11] D. Vashaee, J. Christofferson, A. Shakouri, X. Fan, G. Zeng, C. LaBounty, J. Bowers, and E. Croke, Microscale Thermophys. Eng. (submitted).
[12] L. W. Whitlow and T. Hirano, J. Appl. Phys. **78**, 5460 (1995).
[13] G. D. Mahan and L. M. Woods, Phys. Rev. Lett. **80**, 4016 (1998).
[14] B. Moyzhes and V. Nemchinsky, Appl. Phys. Lett. **73**, 1895 (1998).
[15] C. B. Vining and G. D. Mahan, J. Appl. Phys. **86**, 6852 (1999).
[16] M. D. Ulrich, P. A. Barnes, and C. B. Vining, J. Appl. Phys. **90**, 1625 (2001).
[17] R. J. Radtke, H. Ehrenreich, and C. H. Grein, J. Appl. Phys. **86**, 3195 (1999).
[18] D. Vashaee and A. Shakouri, Phys. Rev. Lett. (submitted).
[19] B. F. Levine, C. G. Bethea, G. Hanian, V. O. Shen, E. Pelve, R. R. Abbott, and S. J. Hsieh, Appl. Phys. Lett. **56**, 851 (1990).
[20] E. Rosencher, F. Luc, Ph. Bois, and S. Delaitre, Appl. Phys. Lett. **61**, 468 (1992).
[21] B. Jogai and K. L. Wang, Appl. Phys. Lett. **46**, 167 (1985).
[22] L. S. Yu, T. H. Wang, S. S. Li, and P. Ho, Appl. Phys. Lett. **60**, 999 (1992).
[23] K. M. S. V. Bandara, R. E. Leibenguth, and M. T. Asom, J. Appl. Phys. **74**, 1826 (1993).
[24] J. L. Pan and C. G. Fonstad, Jr., Mater. Sci. Eng. **28**, 65 (2000).
[25] Y. Shiraishi, N. Furuhata, and A. Okamoto, J. Appl. Phys. **76**, 5099 (1994).
[26] S. V. Meshkov, Sov. Phys. JETP **64**, 1337 (1986).
[27] I. V. Kukushkin and V. B. Timofeev, Pis'ma Zh. Eksp. Teor. Fiz. **40**, 413 (1984) [JETP Lett. **40**, 1231 (1984)].
[28] V. D. Kulakoviskii, B. N. Shepel', A. A. Denisov, and A. P. Senichkin, Fiz. Tekh. Poluprovodn. (S.-Peterburg) **21**, 24 (1987).
[29] E. Pevle, F. Beltram, C. G. Bethea, B'F. Levine, V. O. Shen, S. J. Hsieh, and R. R. Abboth, J. Appl. Phys. **66**, 5656 (1989).
[30] D. Vashaee and A. Shakouri, Mater. Res. Soc. Symp. Proc. **691** (2001).
[31] C. LaBounty, D. Vashaee, X. Fan, G. Zeng, P. Abraham, A. Shakouri, and J. E. Bowers, 19th International Conference on Thermoelectrics, Cardiff, Wales, August 2000.
[32] A. Shakouri, P. Abraham, C. LaBounty, and J. E. Bowers, 17th International Conference on Thermoelectrics, Nagoya, Japan, May 24–28 1998.
[33] S. J. Xu *et al.*, Appl. Phys. Lett. **73**, 3153 (1998).
[34] H. C. Liu, Opto-Electron. Rev. **11**, 1 (2003).
[35] M. Kozhevnikov, V. Narayanamurti, C. Zheng, Y.-J. Chiu, and D. L. Smith, Phys. Rev. Lett. **82**, 3677 (1999).
[36] D. L. Smith, M. Kozhevnikov, E. Y. Lee, and V. Narayanamurti, Phys. Rev. B **61**, 13914 (2000).

[37] D. L. Smith, E. Y. Lee, and V. Narayanamurti, Phys. Rev. Lett. **80**, 2433 (1998).
[38] T. C. Harman, P. J. Taylor, D. L. Spears, and M. P. Walsh, J. Electron. Mater. **29**, L1 (2000).
[39] G. Chen, Semicond. Semimetals **71**, 203 (2001).
[40] R. Venkatasubramanian, Semicond. Semimetals **71**, 175 (2001).
[41] R. Venkatasubramanian, E. Siivola, T. Colpitts, and B. O'Quinn, Nature (London) **413**, 597 (2001).
[42] V. Donchev, J. C. Bourgoin, and P. Bois, Semicond. Sci. Technol. **17**, 621 (2002).
[43] A. Zussman, B. F. Levine, J. M. Kuo, and J. de Jong, J. Appl. Phys. **70**, 5101 (1991).
[44] The mobility, saturation velocity, doping concentration, and barrier height are taken the same as those in Ref. 19: $\mu=600$, 800, 1000, 1200, 2000 $\mathrm{cm}^2/\mathrm{V\,s}$ and $v_s=3$, 3.5, 5, 5.5, 7×10^6 cm/s at $T=112$, 89, 77, 60, and 51 K, respectively. $E_b=245$ meV and $N_D=10^{18}\,\mathrm{cm}^{-3}$.
[45] E. F. Schubert, *Doping in III–V Semiconductors* (Cambridge University Press, New York, 1993).
[46] The mobility and saturation velocity are assumed to be $\mu=700\ \mathrm{cm}^2/\mathrm{V\,s}$ and $v_s=10^7$ cm/s at all given temperatures.
[47] A. Shakouri, I. Grave, Y. Xu, A. Ghaffari, and A. Yariv, Appl. Phys. Lett. **63**, 1101 (1993).
[48] The mobility and saturation velocity are assumed to be $\mu=1000\ \mathrm{cm}^2/\mathrm{V\,s}$ and $v_s=10^7$ cm/s at all given temperatures.